Simultaneous morphology, band structure, and defect optimization of graphitic carbon nitride microsphere by the precursor concentration to boost photocatalytic activity

Shuaijun Wang, Fengting He, Pei Dong, Zhaoxin Tai, Chaocheng Zhao,[a] Yongqiang Wang, and Fang Liu
State Key Laboratory of Petroleum Pollution Control, China University of Petroleum (East China), Qingdao 266580, People's Republic of China

Lin Li
College of Chemical and Environmental Engineering, Shandong University of Science and Technology, Qingdao 266590, People's Republic of China

(Received 2 July 2018; accepted 5 September 2018)

Graphitic carbon nitride (g-C_3N_4) microspheres (CNMS) were fabricated via a solvothermal method by using dicyandiamide and cyanuric chloride as precursors. The morphology, band structure, and defects can be simultaneously regulated by merely adjusting the concentration of precursors. Structural characterization results indicate that all the prepared samples possess spherical morphology, while the band gap decreased as the precursor concentration increased from 8 mmol (CNMS-1) to 24 mmol (CNMS-3). Besides, ultraviolet photoelectron spectroscopy results suggested that the valence band of CNMS-2 (16 mmol) was much higher than that of CNMS-1 and CNMS-3. Additionally, organic elemental analysis, X-ray photoelectron spectroscopy, and electron paramagnetic resonance results unveil the formation of nitrogen defects on the surface of prepared samples. Besides, CNMS-2 exhibits an enhanced apparent reaction rate constant of RhB degradation than that of CNMS-1 and CNMS-3. The improved apparent reaction rate constant may be due to the lowered valence band as well as the formation of nitrogen defects. This work might guide the regulation of the morphology and band structure of g-C_3N_4-based materials prepared via the one-pot hydrothermal method.

I. INTRODUCTION

In the past decades, the energy and environmental crisis have received growing public awareness. To address these problems, semiconductor-based photocatalysis has been used as one of the sustainable approaches owing to its outstanding performances in the H_2 evolution from water, CO_2 photoreduction, and decomposition of organic pollutants.[1–7] The landmark of photocatalytic water splitting using TiO_2 electrodes under ultraviolet (UV) light was ignited by Fujishima and Honda in 1972.[8] Unfortunately, the traditional TiO_2 remains the bottlenecks such as the fast recombination rate of the photogenerated electron–hole pairs and the restricted UV-light response (only about 4% of total sunlight).[9,10] To improve the photocatalytic efficiency, Kako and coworkers used Fe and Ta elements to modify TiO_2 for organic degradation.[11] However, the redox ability is retarded due to the narrowed band gap. Bismuth vanadate ($BiVO_4$) has been an ideal visible light driven semiconductor with a narrow band gap energy of 2.4 eV ($\lambda < 520$ nm).[12] Wei et al. fabricated $BiVO_4$ hierarchical spheres with monoclinic structure via a facile hydrothermal approach.[13] The prepared sample exhibits excellent efficiency toward methylene blue (MB) degradation under visible light irradiation.

Apart from the reported inorganic photocatalysts, graphitic carbon nitride (g-C_3N_4), a metal-free photocatalyst, is of great interest because of its promising electronic property, high environmental stability, and "earth-abundant" nature.[14–16] Besides, g-C_3N_4 can be easily fabricated by thermal polymerization of abundant nitrogen-rich precursors such as melamine, dicyandiamide, cyanamide, urea, thiourea, and ammonium thiocyanate.[17–23] Nevertheless, the prepared bulk g-C_3N_4 still suffers from the high recombination rate of charge carriers and the lack of visible light harvesting.[24,25] Therefore, many strategies have been used to modify bulk g-C_3N_4, such as morphology control,[26] band structure engineering,[27] metal or nonmetal doping,[28] heterojunction construction,[29–31] noble metal deposition,[32] etc. For example, Wang and coworkers reported the fabrication of the C_3N_4/Bi_2WO_6 hybrid via the hydrothermal and calcination methods.[23] In another related work, Chai et al. constructed Ap_3PO_4/C_3N_4 via in situ

[a]Address all correspondence to this author.
e-mail: zhaochch0821@163.com
DOI: 10.1557/jmr.2018.342

 © Materials Research Society 2018

https://doi.org/10.1557/jmr.2018.342 Published online by Cambridge University Press

deposition of Ag_3PO_4 particles on the surface of C_3N_4 sheets.[33] However, the oxidation and reduction powers of charge carriers are restricted because of the charge transfer route. To overcome the drawback of conventional heterojunction photocatalysts, a direct Z-scheme Bi_2O_3/g-C_3N_4 inorganic–organic composite was synthesized by Liu et al. for MB degradation.[34] Meanwhile, Zhang and coworkers developed Z-scheme g-C_3N_4/BiOI heterostructures by a solid phase calcination approach and proposed for the degradation of microcystin-LR.[35] Besides, Feng et al. constructed a Z-scheme MoO_3/g-C_3N_4 photocatalyst via an impregnation method for the photocatalytic CO_2 reduction and RhB degradation.[36] Nevertheless, the stability of the 288.1 hetero components and the durability are challenging to be accomplished.

Elemental doping is another effective way to tune the optical and electronic properties of g-C_3N_4. Luo and coworkers reported a series of B/P/F doped g-C_3N_4 photocatalysts by a facile one-step heating method for photocatalytic H_2 evolution.[37] The prepared samples increased the interplanar stacking distance, enlarged the optical absorption range, and improved the photocatalytic activity of H_2 evolution. Besides, noble metal deposition has also received noticeable research attention owing to its excellent electronic and optical characteristics. The work of Lü and coworkers reported the loading of Ag on the g-C_3N_4 sheet via a simple wet-chemical pathway for the decolorization of methyl orange (MO).[38] The enhanced photocatalytic activity is predominately due to the increased absorption of visible light in terms of surface plasmon resonance effect and electron traps to suppress the recombination of photogenerated electron and hole pairs.

Apart from the strategies mentioned above, the design of g-C_3N_4 with microsphere structure and enhanced visible light harvesting ability is also an effective way to inhibit charge carrier recombination.[40–44] To date, several groups have demonstrated that the construction of g-C_3N_4 microspheres (CNMS) with a broader range of visible light absorption is feasible. For example, Jun and coworkers successfully fabricated g-C_3N_4 hollow spheres using melamine–cyanuric acid complex with the aid of dimethyl sulfoxide.[41] The prepared photocatalyst exhibits enhanced light adsorption, enlarges band gap, and increases the lifetime of photoexcited charge carriers. Gu et al. synthesized hierarchical g-C_3N_4 hollow spheres via the one-step solvothermal method followed by post-heating treatment.[39] In comparison with the bulk g-C_3N_4, the hierarchical g-C_3N_4 microspheres show narrowed band gap and dramatically enhanced photocatalytic activity toward H_2 evolution from the water. Inspired by the aforementioned reported studies, our group found that the morphology, optical, and electronic properties of g-C_3N_4 microspheres can be simultaneously optimized by simply adjusting the solvothermal temperature.[44] However, the morphology, band structure, defects, and photocatalytic activity of CNMS need to be further optimized, and to the best of our knowledge, no study has carried out to regulate the morphology, band structure, and defects of CNMS by changing the concentration of precursors via the one-pot hydrothermal method.

Herein, we report a facile method to tailor the morphology, band structure, and defects of CNMS by adjusting the precursor concentration from 8 mmol to 24 mmol (denoted as CNMS-1, CNMS-2, and CNMS-3, respectively). Structural characterization results indicate that all the prepared samples possess spherical morphology, while the band gap decreased as the precursor concentration increased from 8 mmol (CNMS-1) to 24 mmol (CNMS-3). Also, ultraviolet photoelectron spectroscopy (UPS) results suggested that the valence band of CNMS-2 (16 mmol) was much lower than those of CNMS-1 and CNMS-3 and thus possesses higher photo-oxidation capability. Accordingly, CNMS-180 exhibits higher photocatalytic degradation efficiency on Rhodamine B, stronger photocurrent response, and lower charge transfer resistance.

II. MATERIALS AND METHODS

A. Materials

Dicyandiamide, cyanuric chloride, acetonitrile, bisphenol A (BPA), RhB, MB, and MO were obtained from Sinopharm Chemical Reagent Co., Ltd., China. All chemicals were of analytical grade.

B. Preparation of CNMS

The CNMS was fabricated using a solvothermal approach according to the literature with some modification.[21] In detail, different concentrations of dicyandiamide and cyanuric chloride (8, 16, and 24 mmol) were dissolved in 60 mL of acetonitrile with a mole ratio of 1:2, and the mixture was stirred overnight. Then, the mixture solution was transferred to a 100 mL Teflon-lined autoclave, and then the mixture was sealed and maintained at 180 °C for 24 h. After natural cooling and washing, the final products were obtained.

The working electrodes for the photoelectrochemical experiment were prepared on fluorine-doped tin oxide (FTO) glass. Typically, an FTO glass with 2 cm × 3 cm size was washed with acetone, ethanol, and double distilled water with the aid of sonication. The boundary of FTO glass was protected using a Scotch tape (photoactive area 1 cm^2). By dispersing 10 mg of the as-prepared photocatalyst and 40 μL of Nafion solution into 0.5 mL of ultrapure water, the slurry was coated onto the cleaned FTO glass electrode. The working electrodes were dried under air overnight, and then, the Scotch tape was removed.

https://doi.org/10.1557/jmr.2018.342 Published online by Cambridge University Press

C. Characterization

The morphology was examined on a field-emission scanning electron microscope (FE-SEM, Hitachi Ltd., Tokyo, Japan, S4800) operated at 10 kV. X-ray diffraction (XRD) patterns of the powders were measured using a Holland X'Pert Pro diffractometer. Fourier transform infrared (FT-IR) spectra were collected on a Nicolet Nexus 670 spectrometer in a range of 400–4000 cm^{-1} (Thermo Nicolet Corporation, Waltham, Massachusetts). The Brunauer–Emmett–Teller (BET) surface area was measured using a Micromeritics sorption analyzer (ASAP 2010, Micromeritics Instrument Corporation, Norcross, Georgia). The UV-vis diffuse reflectance spectra (DRS) were recorded on a TU-1901 spectrometer with $BaSO_4$ as a reflectance standard (Beijing Puxi General Instrument Corp., Beijing, China). X-ray photoelectron spectroscopy (XPS) was performed on a PHI 5000CESCA spectrometer equipped with an Mg anode. Hitachi F-4500 Fluorescence spectrophotometer (Hitachi Ltd., Tokyo, Japan) was used to record photoluminescence (PL) spectra of the powders (excitation wavelength of 320 nm). Electron-spin-resonance (ESR) experiments (Bruker A200) were performed using 5,5-dimethyl-1-pyrrolidine-*N*-oxide (DMPO) as a spin-trapping agent. Electron paramagnetic resonance (EPR) experiments (Bruker A200, Bruker, Karlsruhe, Germany.) were performed for the powder samples (Microwave Power 1 mW, sample mass 25 mg, receiver gain 600).

The photoelectrochemical performance of prepared samples was evaluated using a CHI-660 B electrochemical system (Shanghai Huachen Instrument Corp., Shanghai, China). A standard three-electrode cell was used, with the prepared samples/FTO as the working electrode, a saturated calomel electrode as the reference electrode, and a platinum wire as the counter electrode. A 0.1 M $NaSO_4$ solution was selected as an electrolyte. The visible irradiation was obtained from a 300 W Xe lamp (Institute of Perfect Light sources, Beijing, China) with a 420 nm cut-off filter. The photocurrent of the prepared catalysts with visible light irradiation on and off was carried out at a bias of 0.0 V. The electrochemical impedance spectra (EIS) were measured at the open circuit potential, with a sinusoidal AC perturbation of 5 mV applied to the electrode over the frequency range of 0.05–10^5 Hz.

D. Photocatalytic activity test

Photocatalytic activity of the CNMS samples was evaluated by the photocatalytic decomposition of RhB (10 mg/L) solution under visible-light irradiation at room temperature. A 300 W simulated solar Xe lamp (Institute of PerfectLight sources, Beijing) with a 420 nm cut-off filter was used as the visible light source, whose average visible light intensity was 80 mW/cm^2. For each experiment, 25 mg of the powder photocatalyst was added into 50 mL of RhB aqueous solution. Prior to the light irradiation, the suspensions were mechanically stirred in the dark for 30 min to achieve the adsorption–desorption equilibrium. After the xenon lamp was turned on, 3.0 mL suspensions were sampled at given time intervals and filtered through a 0.45 μm Millipore filter to remove the particles. The absorbance of MB (10 mg/L), RhB (10 mg/L), and MO (10 mg/L) was determined at the wavelengths of 664, 553, and 460 nm using a UV-vis spectrophotometer (TU-1901), respectively. The concentration of BPA was detected using high-performance liquid chromatography (HPLC Waters 1525) equipped with an Agilent Zorbax Eclipse Plus C18 column (250 mm × 4.6 mm, 5 μm, USA) and a UV detector (Waters 2489). The mobile phase was acetonitrile and water mixture (60:40, v/v) at a flow rate of 1 mL/min and a constant temperature of 25 °C. The injection volume was 20 μL, and the detection wavelengths applied for BPA is 276 nm.

III. RESULTS AND DISCUSSION

A. Characterization

The morphology and microstructure of the prepared samples are shown in Fig. 1. As shown in Fig. 1, CNMS-1, CNMS-2, and CNMS-3 all exhibit a spherical structure, and the average diameter of CNMS-1, CNMS-2, and CNMS-3 was approximately 2 μm.

Figure 2(a) shows XRD patterns of the CNMS-1, CNMS-2, and CNMS-3. All the samples exhibited a characteristic reflection at the approximately 2θ value of 27.3°, which were assigned to the (002) interlayer of g-C_3N_4.[45,46] However, the characteristic peaks at 13° did not appear, suggesting the existence of structural defects in the CNMS framework.[47] This phenomenon indicates that precursor concentration (from 8 to 24 mmol) is sufficient to polymerize dicyandiamide and cyanuric chloride into g-C_3N_4.

Figure 2(b) shows the FT-IR spectra of the CNMS-1, CNMS-2, and CNMS-3. The absorption bands at 1200–1700 cm^{-1} were because of aromatic CN stretching, and the absorption band at 812 cm^{-1} originated from the breathing mode of the triazine units.[48] In addition, the broad absorption band between 3000 and 3600 cm^{-1} were attributed to N–H and O–H stretching vibration bonds.[49] The above results indicate that the polymerization of cyanuric chloride and dicyandiamide occurred during the solvothermal process.

Figure 2(c) exhibits nitrogen adsorption–desorption isotherms of the CNMS-1, CNMS-2, and CNMS-3 photocatalysts. The prepared samples exhibit type-IV isotherms with H3 loops, which indicates that they possess mesopores and slit-shaped pores. The desorption pore size distribution of prepared photocatalysts is shown in Fig. 2(d), and all the

https://doi.org/10.1557/jmr.2018.342 Published online by Cambridge University Press

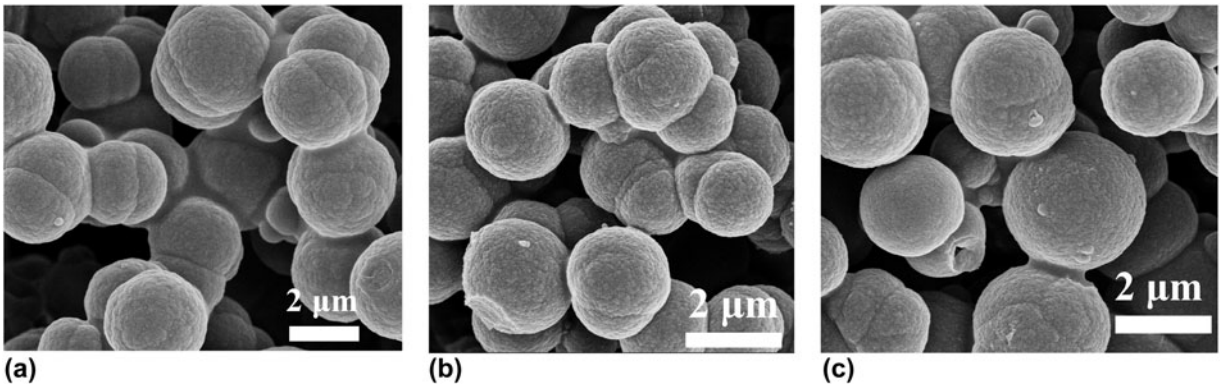


FIG. 1. SEM images of (a) CNMS-1; (b) CNMS-2; (c) CNMS-3.

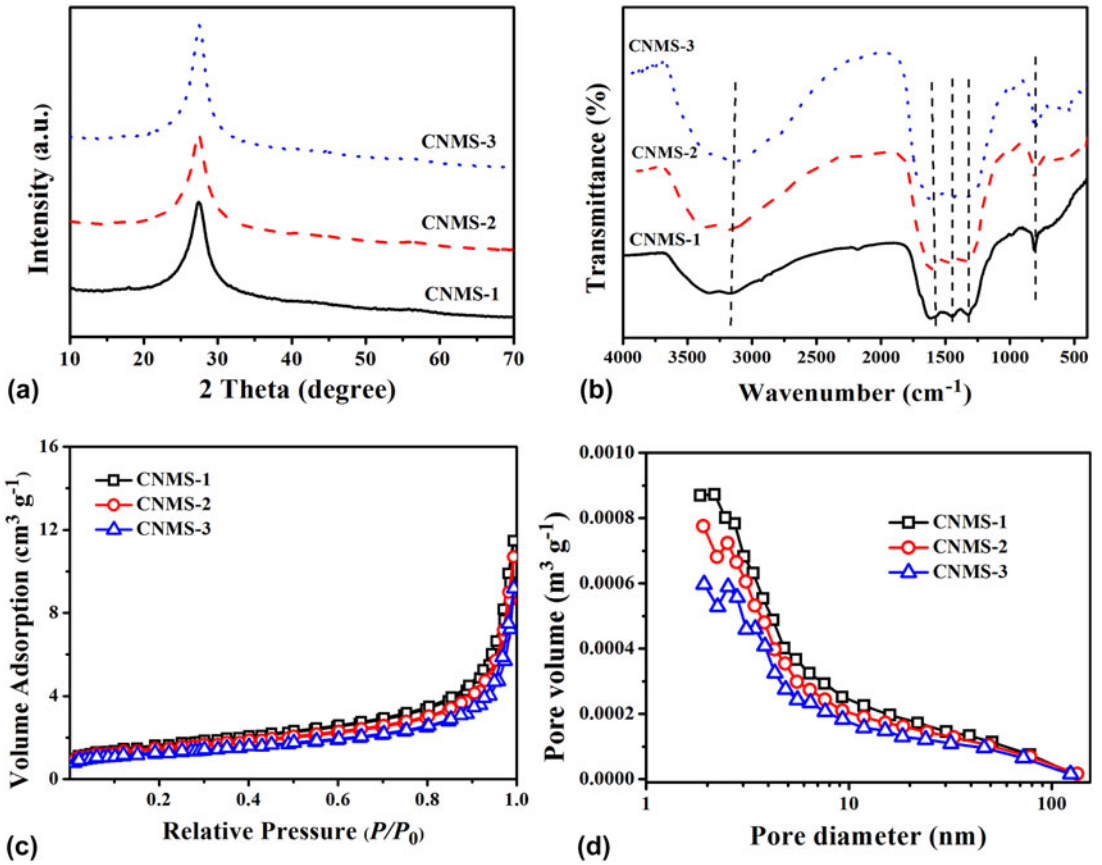


FIG. 2. (a) Powder-XRD patterns; (b) FT-IR spectra; (c) nitrogen adsorption–desorption isotherm, and (d) pore size distribution of CNMS-1, CNMS-2, and CNMS-3.

TABLE I. S_{BET}, pore size, and pore volume of the prepared samples.

Samples	S_{BET} (m^2/g)	Pore size (nm)	Pore volume (cm^3/g)
CNMS-1	5.6	12.9	0.018
CNMS-2	5.0	14.6	0.016
CNMS-3	4.3	13.8	0.014

prepared photocatalysts show a centralized distribution in a 3.5–4 nm range. The BET surface area, pore size, and pore volume of prepared samples are shown in Table I. All the prepared samples exhibit little surface area; therefore, the surface area was not the main reason for the enhancement activity of the CNMS-2.

To further investigate the effects of the precursor concentration on the bulk and surface elemental composition of CNMS, organic elemental analysis (OEA) and XPS measurements were performed. The C/N atomic ratios for CNMS-1, CNMS-2, and CNMS-3 determined from OEA and XPS are listed in Table II. According to XPS, the surface C/N atomic ratio of CNMS-2 was

https://doi.org/10.1557/jmr.2018.342 Published online by Cambridge University Press

TABLE II. The surface C/N atomic ratios are obtained based on the XPS data, and the bulk C/N atomic ratios are from the element analyzer.

Samples	OEA (C/N)	XPS (C/N)
CNMS-1	0.69	1.36
CNMS-2	0.71	1.59
CNMS-3	0.72	1.33

higher than that of CNMS-1 and CNMS-3, indicating CNMS-2 possesses more surface nitrogen vacancies. The OEA results demonstrate that all the samples possess approximately similar C/N atomic ratio, which was close to the theory value (0.75). Therefore, the nitrogen defects mainly located on the surface of CNMS.

To confirm the chemical state of prepared samples, narrow scan C 1*s* and N 1*s* were observed on the surface of all the prepared samples [Fig. 3(a)]. The C 1*s* peak [Fig. 3(b)] can be fitted into two central peaks. The first peak at 288.1 eV was due to graphitic sp^2-bonded carbon in the s-triazine units (N–C=N), and the second peak at approximately 288.7 eV was ascribed to sp^2 graphitic carbon (C–C bonding).[50] The minor C 1*s* peak at 286.1 eV might be due to the N–C(NH)–O units.[40] Consistently, the N 1*s* signals in Fig. 3(c) can also be deconvoluted into three peaks. The central peak at 398.6 eV was attributed to the C–N=C groups, whereas the peak at 400.1 and 401.1 eV corresponded to bridging nitrogen atoms N–$(C)_3$ and amino function C–N–H, respectively.[48]

Figure 4(a) shows the UV-vis DRS of the CNMS-1, CNMS-2, and CNMS-3 samples. In comparison to CNMS-1 and CNMS-3, a slight bathochromic shift of the absorption wavelength is observed in the CNMS-2. In addition, the band gap of the samples was determined using the Kubelka–Munk equation, where $(F(R)h\nu)^{1/2}$ (in which $F(R)$, h, and ν are diffuse absorption coefficient, Planck constant, and light frequency, respectively.) is plotted versus photon energy ($h\nu$) [Fig. 4(b)]; the band gaps of CNMS-1, CNMS-2, and CNMS-3 are estimated at 2.04, 2.0, and 1.95 eV, respectively. Additionally, the valence band energy (E_{VB}) maxima of CNMS were further calculated by the UPS. According to the previously reported literature,[51] the E_{VB} can be estimated by subtracting the full width of the He I UPS spectra [from the highest kinetic energy to the low kinetic energy cutoff, shown in Fig. 4(c)] from the excitation energy ($h\nu$), and thus the valence band energy (E_{CB}) is equal to $E_{VB} - E_g$. By the reference standard [−4.44 eV versus vacuum level equals 0 V versus normal hydrogen electrode (NHE)], the E_{CB} and E_{VB} values in electron volts can be further converted to electrochemical energy potentials in volts.[52] In this case, the E_{VB} of CNMS-1, CNMS-2, and CNMS-3 was estimated to be 2.52, 3.12, and 2.62 V (versus NHE), respectively, and the E_{CB} was determined to be 0.47, 1.12, and 0.67 V (versus NHE),

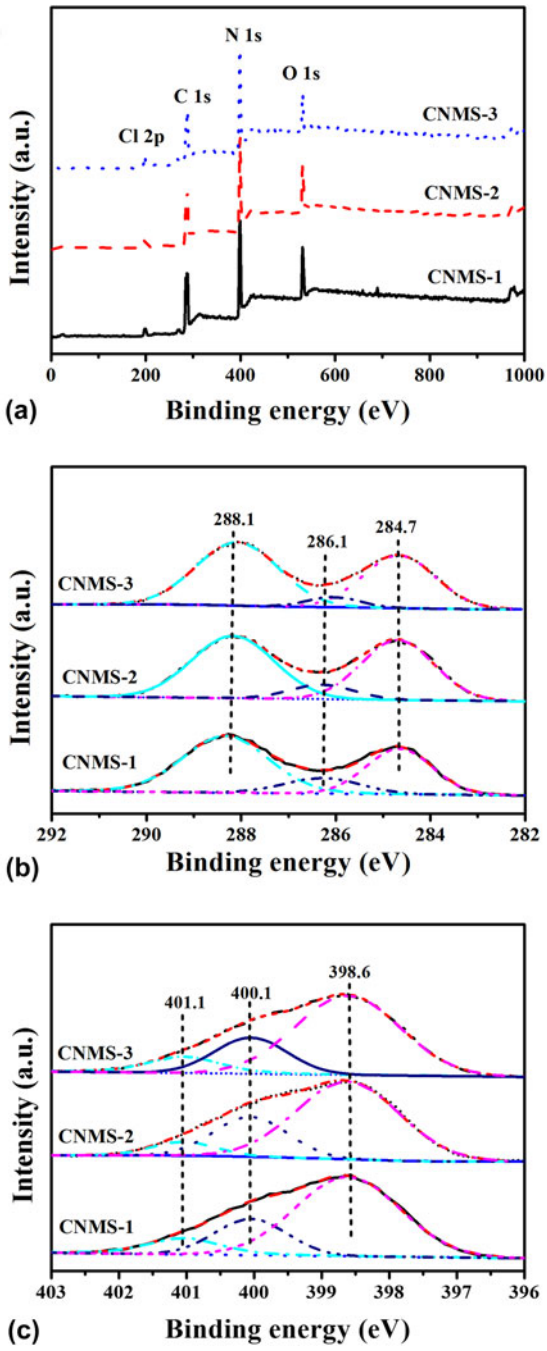


FIG. 3. The (a) XPS spectrum; (b) C1*s*; (c) N1*s* of prepared samples.

respectively. The corresponding band structures of CNMS samples are depicted in Fig. 4(d). The detailed band structure parameters of CNMS-1, CNMS-2, and CNMS-3 are shown in Table III.

Meanwhile, the separation of photoinduced electron–hole pairs played an essential role during the photocatalytic process. Herein, EIS [Fig. 5(a)] was carried out to investigate the process of electron transfer. The arc radius on the EIS Nyquist plot is relevant to the charge transfer resistance, and the large arc radius indicates the

https://doi.org/10.1557/jmr.2018.342 Published online by Cambridge University Press

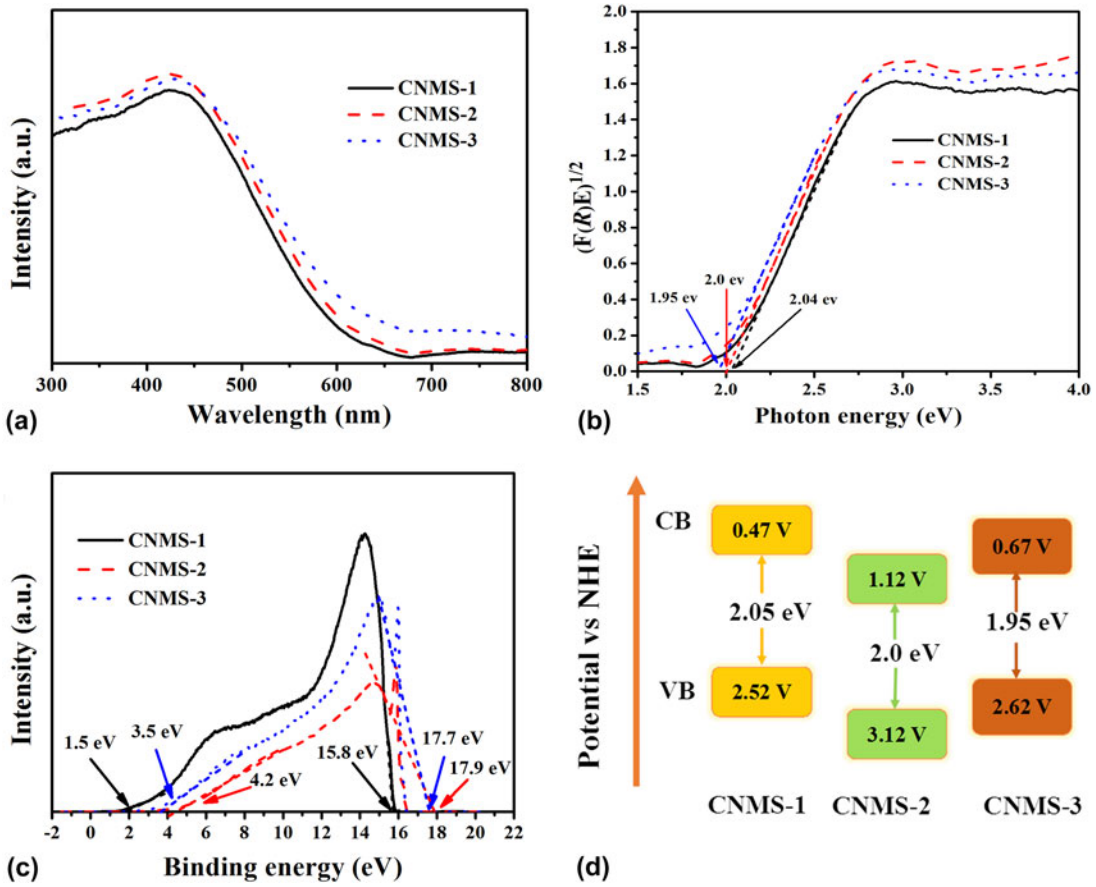


FIG. 4. (a) UV-vis diffuse reflection spectra; (b) the band gap determination plots; (c) UPS spectra; (d) schematic band gap structure of CNMS-1, CNMS-2, and CNMS-3.

TABLE III. Band structure parameters of the CNMS-1, CNMS-2, and CNMS-3.

Samples	E_g (eV)	HKE (eV)	LKE (eV)	$h\nu$ (eV)	E^e (eV)	E_{VB} (V)	E_{CB} (V)
CNMS-1	2.05	15.8	1.5	21.22	4.44	2.52	0.47
CNMS-2	2.0	17.9	4.2	21.22	4.44	3.12	1.12
CNMS-3	1.95	17.7	3.5	21.22	4.44	2.62	0.67

Calculation of the band edges of CNMS-1, CNMS-2, and CNMS-3.
Vacuum level:
$E_{VB} = h\nu - (\text{HKE} - \text{LKE})$.
$E_{CB} = E_{VB} - E_g$.
NHE:
$E_{VB} = E_{VB}$ (versus vacuum level) $- E^e$.
$E_{CB} = E_{CB}$ (versus vacuum level) $- E^e$.
E_g: Band gap.
E_{VB}: Valence band energy.
E_{CB}: Conduction band energy.
HKE: Highest kinetic energy.
LKE: Low kinetic energy.
$h\nu$: Excitation energy.
E^e: The energy of free electrons on the hydrogen scale.

charge transfer limiting process, and vice versa.[53] The Nyquist arc radius of CNMS-2 was smaller than those of CNMS-1 and CNMS-3, which suggests that CNMS-2 exhibits more efficient photoinduced electron and hole separation. Besides, the photocurrent responses of the CNMS-1, CNMS-2, and CNMS-3 are shown in Fig. 5(b). The CNMS-1 photocatalyst presents little photocurrent response, while CNMS-2 and CNMS-3 exhibit obvious

https://doi.org/10.1557/jmr.2018.342 Published online by Cambridge University Press

photocurrent under visible light irritation. The enhancement of photocurrent density in the CNMS-2 sample probably owing to the sufficient condensation and the suitable band gap edges, which contributed to the better separation of photoinduced charge carriers. EPR measurement was carried out to analyze the structural defects. As shown in Fig. 5(c), the tensor parameter (g) of the CNMS-1, CNMS-2, and CNMS-3 is 1.9947, which was due to the unpaired electrons on π-conjugated carbon nitride aromatic rings.[54] Meanwhile, the PL spectra of CNMS-1, CNMS-2, and CNMS-3 were tested at room temperature. As shown in Fig. 5(d), the emission peaks at approximately 455 nm of CNMS-2 were weaker than those of CNMS-1 and CNMS-3, suggesting that the recombination of electrons and holes was effectively inhibited.

B. Photocatalytic activity of the samples

The photocatalytic activities of CNMS-1, CNMS-2, and CNMS-3 were evaluated by the decomposition of RhB under visible light irradiation [Fig. 6(a)]. After 60 min of visible light irradiation, all the samples exhibit approximately 99% degradation efficiency toward RhB, but the decomposition efficiency of CNMS-2 was much higher than that of CNMS-1 and CNMS-3 within 30 min. In addition, the kinetic behaviors of CNMS-1, CNMS-2, and CNMS-3 were investigated further. Figure 6(b) exhibits the apparent reaction rate constant (k) of the prepared samples for the photocatalytic decomposition of RhB. The k value of CNMS-2 was higher than that of CNMS-1 and CNMS-3. The increased k value can be explained by the following two reasons. First, the valence band of CNMS-2 was lower than those of CNMS-1 and CNMS-3; thus, in this case, the oxidation activity of the hole (h^+) was stronger than those of CNMS-1 and CNMS-3. In addition, proper nitrogen vacancies are favorable for the photocatalytic activity. Figure 6(c) exhibits the comparison of photodegradation of RhB (10 mg/L), MO (10 mg/L), MB (10 mg/L), and BPA (3 mg/L). CNMS-2 shows approximately 99% RhB, MB, and MO degradation rate within 60 min. In addition, around 83% of BPA could also be degraded by CNMS-2 within 80 min under the same conditions. These experimental facts indicated that the CNMS-2 photocatalyst could effectively degrade different kinds of organic pollutants and is likely to be a prospective alternative applied in wastewater treatment. The recycling experiment was carried out to verify the stability of CNMS-2

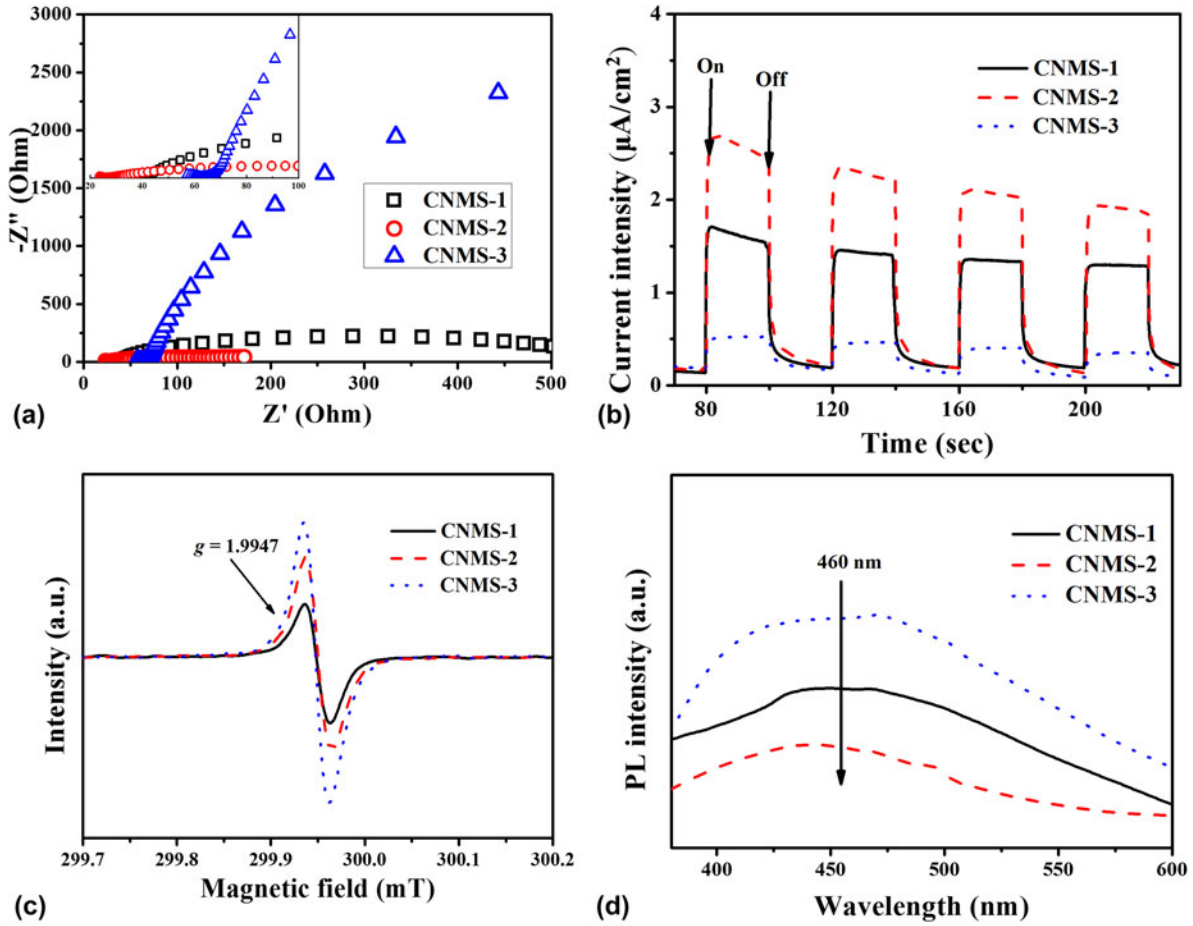


FIG. 5. (a) EIS; (b) photocurrent under visible light; (c) EPR signals; and (d) PL spectra of the prepared samples.

https://doi.org/10.1557/jmr.2018.342 Published online by Cambridge University Press

under visible light irradiation. As shown in Fig. 6(d), the photocatalytic activity of the CNMS-2 catalyst exhibits little decrease after four successive runs, indicating the excellent stability of the CNMS-2 catalyst.

Previously reported studies indicated that h^+, •OH, and $•O_2^-$ are detected in the g-C_3N_4 based system.[55,56] Besides, in this work, we carried out ESR analysis for the detection of active species in water and methanol, respectively. As shown in Figs. 7(a) and 7(b), no ESR signals for CNMS-2 were observed in the dark. Under visible light irradiation, the ESR signals with an intensity ratio of 1:1:1:1 and with a characteristic of 1:2:2:1 are for DMPO-$•O_2^-$ and DMPO-•OH, respectively. Based on the previously reported studies and ESR result, h^+, •OH, and

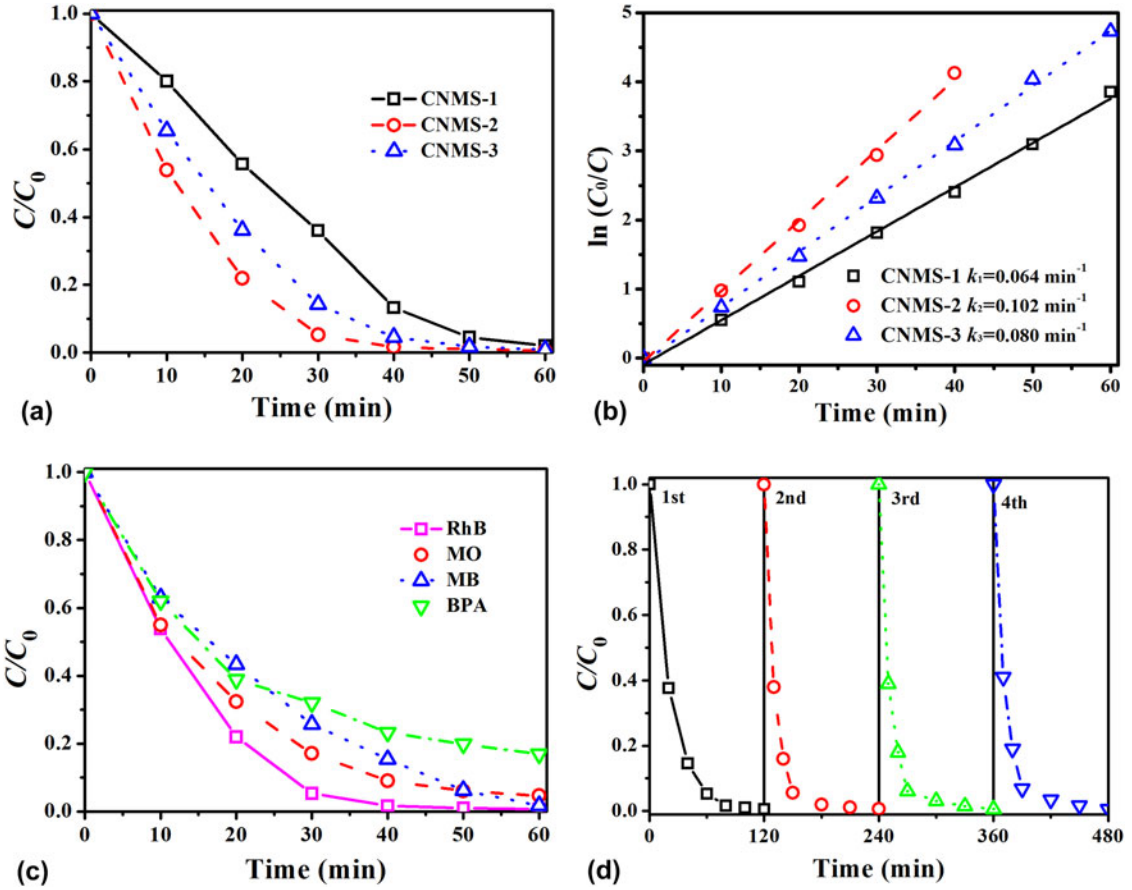


FIG. 6. (a) Photocatalytic degradation of RhB; (b) the first-order-kinetic plots of CNMS-1, CNMS-2, and CNMS-3; (c) the photocatalytic degradation efficiency of CNMS-2 toward MB, RhB, MO, and BPA; and (d) the stability of the CNMS-2 catalyst.

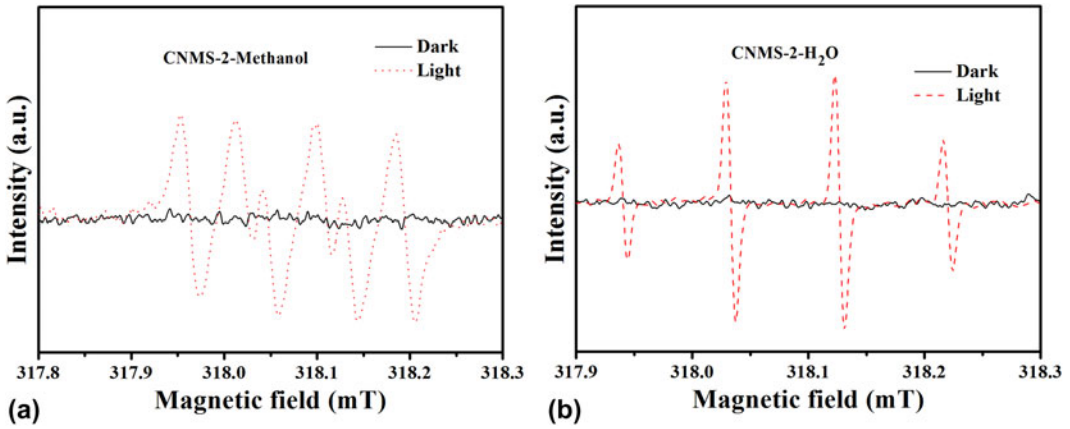


FIG. 7. ESR spectra of (a) CNMS-2 in methanol and (b) CNMS-2 in water.

https://doi.org/10.1557/jmr.2018.342 Published online by Cambridge University Press

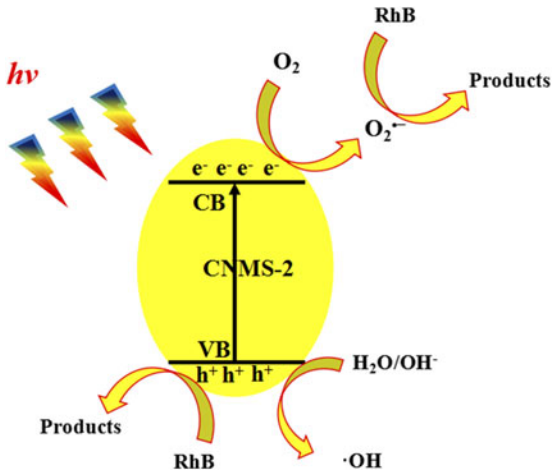


FIG. 8. Schematic illustration of a proposed mechanism for the CNMS-2 system.

$\cdot O_2^-$ are the main active species. Besides, a tentative mechanism for CNMS-2 was proposed in Fig. 8.

IV. CONCLUSIONS

In summary, we have prepared g-C_3N_4 microspheres via a template-free solvothermal method. The morphology, band structure, and defects were simultaneously tailored by simply adjusting the concentration of precursors. Structural characterization results indicate that all the prepared samples possess spherical morphology, while the band gap decreased as the precursor concentration increased from 8 mmol (CNMS-1) to 24 mmol (CNMS-3). In addition, UPS results suggested that the valence band of CNMS-2 (16 mmol) was much higher than those of CNMS-1 and CNMS-3 and thus possesses higher photo-oxidation capability. Consequently, CNMS-2 exhibits higher photocatalytic degradation efficiency on Rhodamine B degradation within 30 min. Additionally, OEA, XPS, and EPR results unveil the formation of nitrogen defects on the surface of prepared samples.

ACKNOWLEDGMENTS

This work was financially supported by the National Science and Technology Major Project (No. 2016ZX05040003) and the Fundamental Research Funds for the Central Universities (Nos. 17CX06027 and 18CX06068A).

REFERENCES

1. J. Wang, C. Qin, H. Wang, M. Chu, A. Zada, X. Zhang, J. Li, F. Raziq, Y. Qu, and L. Jing: Exceptional photocatalytic activities for CO_2 conversion on Al–O bridged g-C_3N_4/α-Fe_2O_3 Z-scheme nanocomposites and mechanism insight with isotopesZ. *Appl. Catal., B* **221**, 459 (2018).
2. Y. Tamaki and O. Ishitani: Supramolecular photocatalysts for the reduction of CO_2. *ACS Catal.* **7**, 3394 (2017).
3. L. Shi, L. Yang, W. Zhou, Y. Liu, L. Yin, X. Hai, H. Song, and J. Ye: Photoassisted construction of holey defective g-C_3N_4 photocatalysts for efficient visible-light-driven H_2O_2 production. *Small* **14**, 1703142 (2018).
4. M. Zhu, S. Kim, L. Mao, M. Fujitsuka, J. Zhang, X. Wang, and T. Majima: Metal-free photocatalyst for H_2 evolution in visible to near-infrared region: Black phosphorus/graphitic carbon nitride. *J. Am. Chem. Soc.* **139**, 13234 (2017).
5. H. Wang, X. Yuan, Y. Wu, G. Zeng, X. Chen, L. Leng, and H. Li: Synthesis and applications of novel graphitic carbon nitride/metal-organic frameworks mesoporous photocatalyst for dyes removal. *Appl. Catal., B* **174–175**, 445 (2015).
6. T. Kanagaraj, S. Thiripuranthagan, S.M.K. Paskalis, and H. Abe: Visible light photocatalytic activities of template free porous graphitic carbon nitride-BiOBr composite catalysts towards the mineralization of reactive dyes. *Appl. Surf. Sci.* **426**, 1030 (2017).
7. X. Li, J. Yu, and M. Jaroniec: Hierarchical photocatalysts. *Chem. Soc. Rev.* **45**, 2603 (2016).
8. K.H.A. Fujishima: Electrochemical photolysis of water at a semiconductor electrode. *Nature*, **238**, 37 (1972).
9. J. Low, B. Cheng, and J. Yu: Surface modification and enhanced photocatalytic CO_2 reduction performance of TiO_2: A review. *Appl. Surf. Sci.* **392**, 658 (2017).
10. Y. Ma, X. Wang, Y. Jia, X. Chen, H. Han, and C. Li: Titanium dioxide-based nanomaterials for photocatalytic fuel generations. *Chem. Rev.* **114**, 9987 (2014).
11. T. Kako, W. Yao, and J. Ye: Preparation and characterization of visible light sensitive Fe- and Ta-codoped TiO_2 photocatalyst. *J. Mater. Res.* **25**, 110 (2011).
12. Y.H. Ng, A. Iwase, A. Kudo, and R. Amal: Reducing graphene oxide on a visible-light $BiVO_4$ photocatalyst for an enhanced photoelectrochemical water splitting. *J. Phys. Chem. Lett.* **1**, 2607 (2010).
13. W. Wei, X. Yue, H. Cui, X. Lü, and J. Xie: Hydrothermal synthesis and properties of $BiVO_4$ photocatalysts. *J. Mater. Res.* **28**, 3408 (2013).
14. W.J. Ong, L.L. Tan, Y.H. Ng, S.T. Yong, and S.P. Chai: Graphitic carbon nitride (g-C_3N_4)-based photocatalysts for artificial photosynthesis and environmental remediation: Are we a step closer to achieving sustainability? *Chem. Rev.* **116**, 7159 (2016).
15. X. She, L. Liu, H. Ji, Z. Mo, Y. Li, L. Huang, D. Du, H. Xu, and H. Li: Template-free synthesis of 2D porous ultrathin nonmetal-doped g-C_3N_4 nanosheets with highly efficient photocatalytic H_2 evolution from water under visible light. *Appl. Catal., B* **187**, 144 (2016).
16. C. Sun, M.H. Zhang, Q.Q. Fei, D.Y. Wang, Z.L. Sun, Z.M. Geng, W.M. Xu, and F. Liu: Graphite-like g-C_3N_4-F127-Au nanosheets used for sensitive monitoring of heat shock protein 90. *Sens. Actuators, B* **256**, 160 (2018).
17. J. Zhu, T. Diao, W. Wang, X. Xu, X. Sun, S.A.C. Carabineiro, and Z. Zhao: Boron doped graphitic carbon nitride with acid-base duality for cycloaddition of carbon dioxide to epoxide under solvent-free condition. *Appl. Catal., B* **219**, 92 (2017).
18. R. He, J. Zhou, H. Fu, S. Zhang, and C. Jiang: Room-temperature in situ fabrication of Bi_2O_3/g-C_3N_4 direct Z-scheme photocatalyst with enhanced photocatalytic activity. *Appl. Surf. Sci.* **430**, 273 (2018).
19. H. Zhang, W. Tian, L. Zhou, H. Sun, M. Tade, and S. Wang: Monodisperse Co_3O_4 quantum dots on porous carbon nitride nanosheets for enhanced visible-light-driven water oxidation. *Appl. Catal., B* **223**, 2 (2018).
20. B. Luo, R. Song, and D. Jing: Significantly enhanced photocatalytic hydrogen generation over graphitic carbon nitride with

https://doi.org/10.1557/jmr.2018.342 Published online by Cambridge University Press

carefully modified intralayer structures. *Chem. Eng. J.* **332**, 499 (2018).
21. F. Dong, Z. Zhao, T. Xiong, Z. Ni, W. Zhang, Y. Sun, and W.K. Ho: In situ construction of g-C_3N_4/g-C_3N_4 metal-free heterojunction for enhanced visible-light photocatalysis. *ACS Appl. Mater. Interfaces* **5**, 11392 (2013).
22. L. Ye, D. Wang, and S. Chen: Fabrication and enhanced photoelectrochemical performance of MoS_2/S-doped g-C_3N_4 heterojunction film. *ACS Appl. Mater. Interfaces* **8**, 5280 (2016).
23. M. Wang, M.H. Fang, C. Tang, L.N. Zhang, Z.H. Huang, Y.G. Liu, and X.W. Wu: A C_3N_4/Bi_2WO_6 organic–inorganic hybrid photocatalyst with a high visible-light-driven photocatalytic activity. *J. Mater. Res.* **31**, 713 (2016).
24. H. Yu, R. Shi, Y. Zhao, T. Bian, Y. Zhao, C. Zhou, G.I.N. Waterhouse, L.Z. Wu, C.H. Tung, and T. Zhang: Alkali-assisted synthesis of nitrogen deficient graphitic carbon nitride with tunable band structures for efficient visible-light-driven hydrogen evolution. *Adv. Mater.* **29**, 1605148 (2017).
25. J. Wen, J. Xie, X. Chen, and X. Li: A review on g-C_3N_4-based photocatalysts. *Appl. Surf. Sci.* **391**, 72 (2017).
26. L. Zhou, H. Zhang, H. Sun, S. Liu, M.O. Tade, S. Wang, and W. Jin: Recent advances in non-metal modification of graphitic carbon nitride for photocatalysis: A historic review. *Catal. Sci. Technol.* **6**, 7002 (2016).
27. J. Barrio, L. Lin, X. Wang, and M. Shalom: Design of a unique energy-band structure and morphology in a carbon nitride photocatalyst for improved charge separation and hydrogen production. *ACS Sustainable Chem. Eng.* **6**, 519 (2017).
28. Q. Wang, W. Wang, L. Zhong, D. Liu, X. Cao, and F. Cui: Oxygen vacancy-rich 2D/2D BiOCl-g-C_3N_4 ultrathin heterostructure nanosheets for enhanced visible-light-driven photocatalytic activity in environmental remediation. *Appl. Catal., B* **220**, 290 (2018).
29. Q. Hao, R. Wang, H. Lu, C. Xie, W. Ao, D. Chen, C. Ma, W. Yao, and Y. Zhu: One-pot synthesis of C/Bi/Bi_2O_3 composite with enhanced photocatalytic activity. *Appl. Catal., B* **219**, 63 (2017).
30. K. He, J. Xie, Z-Q. Liu, N. Li, X. Chen, J. Hu, and X. Li: Multifunctional Ni_3C cocatalyst/g-C_3N_4 nanoheterojunctions for robust photocatalytic H_2 evolution under visible light. *J. Mater. Chem. A* **6**, 13110 (2018).
31. K. He, J. Xie, X. Luo, J. Wen, S. Ma, X. Li, Y. Fang, and X. Zhang: Enhanced visible light photocatalytic H_2 production over Z-scheme g-C_3N_4 nansheets/WO_3 nanorods nanocomposites loaded with $Ni(OH)_x$ cocatalysts. *Chin. J. Catal.* **38**, 240 (2017).
32. S. Samanta, S. Martha, and K. Parida: Facile synthesis of Au/g-C_3N_4 nanocomposites: An inorganic/organic hybrid plasmonic photocatalyst with enhanced hydrogen gas evolution under visible-light irradiation. *ChemCatChem*, **6**, 1453 (2014).
33. B. Chai, F. Zou, and W. Chen: Facile synthesis of Ag_3PO_4/C_3N_4 composites with improved visible light photocatalytic activity. *J. Mater. Res.* **30**, 1128 (2015).
34. S. Liu, J. Chen, D. Xu, X. Zhang, and M. Shen: Enhanced photocatalytic activity of direct Z-scheme Bi_2O_3/g-C_3N_4 composites via facile one-step fabrication. *J. Mater. Res.* **33**, 1391 (2018).
35. F. Zhang, L. Wang, M. Xiao, F. Liu, X. Xu, and E. Du: Construction of direct solid-state Z-scheme g-C_3N_4/BiOI with improved photocatalytic activity for microcystin-LR degradation. *J. Mater. Res.* **33**, 201 (2017).
36. Z. Feng, L. Zeng, Y. Chen, Y. Ma, C. Zhao, R. Jin, Y. Lu, Y. Wu, and Y. He: In situ preparation of Z-scheme MoO_3/g-C_3N_4 composite with high performance in photocatalytic CO_2 reduction and RhB degradation. *J. Mater. Res.* **32**, 3660 (2017).
37. Y. Luo, J. Wang, S. Yu, Y. Cao, K. Ma, Y. Pu, W. Zou, C. Tang, F. Gao, and L. Dong: Nonmetal element doped g-C_3N_4 with enhanced H_2 evolution under visible light irradiation. *J. Mater. Res.* **33**, 1268 (2018).
38. X. Lü, J. Shen, Z. Wu, J. Wang, and J. Xie: Deposition of Ag nanoparticles on g-C_3N_4 nanosheet by N,N-dimethylformamide: Soft synthesis and enhanced photocatalytic activity. *J. Mater. Res.* **29**, 2170 (2014).
39. Q. Gu, Y. Liao, L. Yin, J. Long, X. Wang, and C. Xue: Template-free synthesis of porous graphitic carbon nitride microspheres for enhanced photocatalytic hydrogen generation with high stability. *Appl. Catal., B* **165**, 503 (2015).
40. Q. Gu, Z. Gao, and C. Xue: Self-Sensitized carbon nitride microspheres for long-lasting visible-light-driven hydrogen generation. *Small* **12**, 3543 (2016).
41. Y. Jun, E.Z. Lee, X. Wang, W.H. Hong, G.D. Stucky, and A. Thomas: From melamine-cyanuric acid supramolecular aggregates to carbon nitride hollow spheres. *Adv. Funct. Mater.* **23**, 3661 (2013).
42. J. Sun, J. Zhang, M. Zhang, M. Antonietti, X. Fu, and X. Wang: Bioinspired hollow semiconductor nanospheres as photosynthetic nanoparticles. *Nat. Commun.*, **3**, 1139 (2012).
43. Y. Cui, Y. Tang, and X. Wang: Template-free synthesis of graphitic carbon nitride hollow spheres for photocatalytic degradation of organic pollutants. *Mater. Lett.* **161**, 197 (2015).
44. S. Wang, Q. Yan, P. Dong, C. Zhao, Y. Wang, F. Liu, and L. Li: Morphology and band structure regulation of graphitic carbon nitride microspheres by solvothermal temperature to boost photocatalytic activity. *Appl. Phys. A* **124**, 416 (2018).
45. Z. Zhang, J. Huang, M. Zhang, Q. Yuan, and B. Dong: Ultrathin hexagonal SnS_2 nanosheets coupled with g-C_3N_4 nanosheets as 2D/2D heterojunction photocatalysts toward high photocatalytic activity. *Appl. Catal., B* **163**, 298 (2015).
46. J. Zhang, X. An, N. Lin, W. Wu, L. Wang, Z. Li, R. Wang, Y. Wang, J. Liu, and M. Wu: Engineering monomer structure of carbon nitride for the effective and mild photooxidation reaction. *Carbon* **100**, 450 (2016).
47. Q. Gu, H. Sun, Z. Xie, Z. Gao, and C. Xue: MoS_2-coated microspheres of self-sensitized carbon nitride for efficient photocatalytic hydrogen generation under visible light irradiation. *Appl. Surf. Sci.* **396**, 1808 (2017).
48. Y. Li, M. Yang, Y. Xing, X. Liu, Y. Yang, X. Wang, and S. Song: Preparation of carbon-rich g-C_3N_4 nanosheets with enhanced visible light utilization for efficient photocatalytic hydrogen production. *Small* **13**, 1701552 (2017).
49. H. Lan, L. Li, X. An, F. Liu, C. Chen, H. Liu, and J. Qu: Microstructure of carbon nitride affecting synergetic photocatalytic activity: Hydrogen bonds versus structural defects. *Appl. Catal., B* **204**, 49 (2017).
50. R. Hao, G. Wang, H. Tang, L. Sun, C. Xu, and D. Han: Template-free preparation of macro/mesoporous g-C_3N_4/TiO_2 heterojunction photocatalysts with enhanced visible light photocatalytic activity. *Appl. Catal., B* **187**, 47 (2016).
51. J. Liu, Y. Liu, N. Liu, Y. Han, X. Zhang, H. Huang, Y. Lifshitz, S.T. Lee, J. Zhong, and Z. Kang: Metal-free efficient photocatalyst for stable visible water splitting via a two-electron pathway. *Science* **347**, 970 (2015).
52. X. She, J. Wu, H. Xu, J. Zhong, Y. Wang, Y. Song, K. Nie, Y. Liu, Y. Yang, M-T.F. Rodrigues, R. Vajtai, J. Lou, D. Du, H. Li, and P.M. Ajayan: High efficiency photocatalytic water splitting using 2D α-Fe_2O_3/g-C_3N_4 Z-scheme catalysts. *Adv. Energy Mater.* **7**, 1700025 (2017).
53. X. Bai, L. Wang, Y. Wang, W. Yao, and Y. Zhu: Enhanced oxidation ability of g-C_3N_4 photocatalyst via C_{60} modification. *Appl. Catal., B* **152–153**, 262 (2014).

https://doi.org/10.1557/jmr.2018.342 Published online by Cambridge University Press

54. W. Wu, J. Zhang, W. Fan, Z. Li, L. Wang, X. Li, Y. Wang, R. Wang, J. Zheng, M. Wu, and H. Zeng: Remedying defects in carbon nitride to improve both photooxidation and H_2 generation efficiencies. *ACS Catal.* **6**, 3365 (2016).
55. L. Ye, J. Liu, Z. Jiang, T. Peng, and L. Zan: Facets coupling of BiOBr-g-C_3N_4 composite photocatalyst for enhanced visible-light-driven photocatalytic activity. *Appl. Catal., B* **142–143**, 1 (2013).
56. Q. Hao, X. Niu, C. Nie, S. Hao, W. Zou, J. Ge, D. Chen, and W. Yao: A highly efficient g-C_3N_4/SiO_2 heterojunction: The role of SiO_2 in the enhancement of visible light photocatalytic activity. *Phys. Chem. Chem. Phys.* **18**, 31410 (2016).

https://doi.org/10.1557/jmr.2018.342 Published online by Cambridge University Press